Journal of
Marine Science and Engineering

MDPI

Article

Analysis, Simulation and Experimental Study of the Tensile Stress Calibration of Ceramic Cylindrical Pressure Housings

Peng Wang [1], Yanhui Wang [1,2,3,*], Shaoqiong Yang [1,2,3], Wendong Niu [1,2,3], Xuehao Wang [1] and Penghao Li [2]

1 Key Laboratory Mechanism Theory and Equipment Design of Ministry of Education, School of Mechanical Engineering, Tianjin University, Tianjin 300350, China; peng_wang@tju.edu.cn (P.W.); shaoqiongy@tju.edu.cn (S.Y.); wendongniutj@tju.edu.cn (W.N.); xuehaowang@tju.edu.cn (X.W.)
2 Qingdao Institute for Ocean Engineering, Tianjin University, Qingdao 266237, China; penghaoli@tju.edu.cn
3 The Joint Laboratory of Ocean Observing and Detection, Pilot National Laboratory for Marine Science and Technology (Qingdao), Qingdao 266237, China
* Correspondence: yanhuiwang@tju.edu.cn

Abstract: Engineering ceramics have extremely high values for both specific modulus and specific compressive strength, making them one of the most promising materials for enhancing the carrying capability of full ocean depth (FOD) submersibles. However, due to the low tensile strength of most ceramic materials, the tensile stress generated at the contact surface of ceramic pressure housings under hydrostatic pressure may exceed the material's limits and thus lead to cracking failure. Currently, there are no valid calibration methods for the tensile stress caused by material discontinuities at the contact surface. In this paper, an approximate model is established based on contact mechanics. The absolute error of the approximate model, as verified by the simulation results for nine groups of ceramic pressure housings, does not exceed 14.2%. It is also concluded that the smaller the difference in Young's modulus between the ceramics and metals, the higher the tensile strength safety factor. In addition, two hydrostatic pressure experiments were carried out to further verify the results of the approximate model and the numerical solutions. The approximate model is oriented to the reliable design of ceramic pressure housings. It will play an important role in improving the carrying capacity and observation capability of FOD submersibles.

Keywords: ceramic pressure housing; contact model; tensile strength; full ocean depth

Citation: Wang, P.; Wang, Y.; Yang, S.; Niu, W.; Wang, X.; Li, P. Analysis, Simulation and Experimental Study of the Tensile Stress Calibration of Ceramic Cylindrical Pressure Housings. *J. Mar. Sci. Eng.* **2022**, *10*, 499. https://doi.org/10.3390/jmse10040499

Academic Editors: Weicheng Cui, Lian Lian and Guang Pan

Received: 14 March 2022
Accepted: 1 April 2022
Published: 4 April 2022

1. Introduction

As the deepest and most mysterious part of the ocean, the hadal zone has become a frontier hotspot for marine scientific research [1]. According to UNESCO's classification, the depth of the hadal zone is 6500 m~11,000 m [2]. Despite covering only approximately 1% of the global ocean area, it constitutes nearly 45% of the ocean depth gradient [3]. Extremely high hydrostatic pressure is the most typical feature of the hadal zone and poses significant challenges for FOD submersibles seeking to enter this region [4]. Lightweight, high-strength pressure hulls are essential requirements for FOD submersibles. Due to their extremely high specific modulus and specific compressive strength compared to traditional metal materials, engineering ceramics are of increasing interest [5]. Moreover, not only are pressure housings made of ceramics corrosion-resistant, but they also have no magnetic shielding [6]. This means that engineering ceramics are excellent materials for fabricating pressure housings for FOD submersibles.

At present, many research institutes carry out research on ceramic pressure housings or use them in scientific applications. For example, Stachiw et al. designed a ceramic pressure housing with metal U-rings bonded to both ends of a ceramic cylindrical shell and matched with two hemispherical metal end-caps [7]. Subsequently, they conducted extensive experimental studies on ceramic pressure hull design with funding from the Naval Center for Combat and Operational Stress Control (NCCOSC); their goal was the application of ceramic pressure housings for use in unmanned and manned submersibles [7]. The Woods Hole Oceanographic Institution (WHOI) developed the 11,000 m-class "Nereus" hybrid remote operated vehicle (HROV) using two different sizes of Al_2O_3 ceramic pressure housings for installing energy-related components, electronics, and cameras [8]. The Japan Agency for Marine-Earth Science and Technology (JAMSTEC) developed a 6000 m-class virtual mooring underwater glider with an Al_2O_3 ceramic pressure housing [9]. The above-mentioned ceramic pressure housings all adopt a cylindrical shape with a metal end-cap at each end. Spherical ceramic shells are mainly used as buoyancy spheres [10,11] and, to a lesser extent, as pressure housings for ocean-bottom seismometers [12]. However, ceramic pressure housings are not widely used.

As brittle materials, the tensile strength of most ceramic materials is only approximately 10% of their compressive strength; tensile strength is one of their weakest properties. Stachiw et al. [13] and McDonald et al. [14] both mention the problem in their studies, pointing out that the most common failure under hydrostatic pressure is ceramic shell end cracking. The mechanical properties of ceramic and metal on both sides of the contact surface are different, resulting in uncoordinated tangential deformation along the contact surface under external pressure, which leads to the generation of tensile stress. When the tensile stress exceeds the ceramic material's limitation, cracks develop at the end of the shell and extend to the other end [15]. The above-mentioned studies analyzed the problem qualitatively and provided valuable structural designs as well as empirical safety factors. In addition, many studies on improving the toughness and compressive strength of ceramic materials have been carried out [16,17]. However, there is still a lack of theoretical studies concerning the calibration of the tensile stress on the ceramic shell end faces.

From a theoretical perspective, the contact between the ceramic shell and metal under hydrostatic pressure can be regarded as a flat annular indenter pressed into the elastic half-space. The problem is a mixed boundaries problem with three regions. Collins et al. reduced the problem to a Fredholm integral equation and solved it by the iterative method [18]. Toshikazu et al. transformed the problem into solving an infinite set of simultaneous equations by assuming the pressure distribution on the contact surface [19]. These studies treat the contact model as frictionless and the indenter as infinitely rigid. In addition, based on frictionless contact solutions, the adhesive contact [20], slip contact [21], and rough contact [22] problems have been further investigated. In fact, most of the studies treat the annular indenter as an infinitely rigid body to study the contact mechanics of elastic bodies. However, the contact mechanics of indenters ignored by most contact models are critical for ceramic pressure housings. Although Hertzian contact theory is a valid method for analyzing the contact mechanics of two actual elastic objects, it is not applicable to plane-to-plane contact problems [21]. Jordan et al. proposed an approximate method to analyze the contact mechanics of a cylindrical flat indenter with finite rigidity but did not extend their efforts to a flat annular indenter [23].

In this paper, we focus on the analysis of the contact mechanics of ceramic cylindrical pressure housings. An approximate contact mechanics model, considering the actual stiffness of ceramic materials and the practical structure, is established based on elastic mechanics theory. The approximate model is implemented in the following steps. First, the pressure distribution on the contact surface of the ceramic shell is estimated by adding a force balance coefficient to the pressure distribution of the frictionless, infinitely stiff flat annular indenter contact model. The force balance coefficient contains the stiffness parameters of the two contact materials. Second, a frictionless contact model for a finitely rigid flat annular indenter is obtained using the frictionless, infinitely rigid flat annular indenter contact model and the estimated pressure distribution. Finally, a structure coefficient is added to approximate the practical pressure housing. The coefficient is a determined value solved by a numerical method and has acceptable accuracy for ceramic pressure housings under the same design requirements. Meanwhile, finite element method (FEM) simulations for nine groups of ceramic pressure housings and hydrostatic pressure experiments for two groups are carried out for comparison and verification.

The main part of this paper is divided into the following sections. In Section 2, the cracking failure of ceramic pressure housings due to tensile stress on the ceramic contact surface is described in terms of material properties and structure design. In Section 3, to calibrate the tensile stress on the ceramic contact surface, an approximate contact model is established based on a contact mechanics model. In Section 4, nine groups of ceramic pressure housings are derived for approximate model validation based on three typical metals and three typical ceramic materials. Their dimensions are determined by calibrating the compressive strength and buckling under the same preliminary design conditions. FEM simulations for nine groups of housings are performed for the validation of the approximate model. In Section 5, the comparison and discussion of the results of the approximate model calculations and FEM simulations are carried out. Two sets of pressure experiments are conducted to verify the calculation and simulation results. Finally, the conclusions are summarized in Section 6.

2. Problem Description

The most common failure of ceramic pressure housings is ceramic contact face cracking. This is due to the tensile stress on the ceramic contact face under hydrostatic pressure exceeding the permissible limits of the material. The main reasons for the overload of the tensile stress are: (1) the properties of the ceramic materials and (2) the structural designs of the ceramic pressure housings.

2.1. Material Properties

Table 1 shows the properties of three typical ceramic materials and three typical metal materials.

Table 1. Properties of ceramic materials and metal materials.

Materials	Specific Gravity (g/cm^3)	Young's Modulus (GPa)	Compressive Strength (MPa)	Tensile Stress (Yield) (MPa)	Poisson's Ratio
Al_2O_3 (99%)	3.9	390	2160	310	0.23
Si_3N_4	3.2	310	2810	810	0.27
SiC	3.12	440	3400	340	0.18
Aluminum 7075-T6	2.78	71	480	480	0.33
Titanium TC4	4.45	110	900	900	0.3
Steel 17-4PH	7.89	207	1160	1160	0.28

The comparative results of the mechanical properties and load-bearing properties of the listed materials are shown in Figure 1. Ceramic materials have extremely high Young's modulus/specific modulus and compressive strength/specific compressive strength compared to metal materials. This indicates that the ceramic housings have better structural stability and compressive stress safety factor under external hydrostatic pressure. Their high specific strength and modulus further prove the superiority of their load-bearing properties. However, the tensile strengths of the SiC ceramic and the Al_2O_3 ceramic are only approximately 10% of their compressive strength. Only the tensile strength of Si_3N_4 ceramic is higher; at 29% of its compressive strength, it is nearly the same as TC4 and 17-4PH. The design of pressure housings follows the "Bucket Law", meaning that their performance is determined by the weakest mechanical property. The compressive and tensile strengths of metal materials are very close. Metal housings are usually composed of a single homogeneous material and are generally not subject to tensile stress under hydrostatic pressure. Therefore, the pressure vessel design standards do not consider tensile stress calibration in designing metal housings. However, more attention should be given to the tensile stress calibration for ceramic pressure housings, as low tensile strength is an inherent weakness of ceramic materials. The calibration of tensile stress follows the maximum principal stress theory [24].

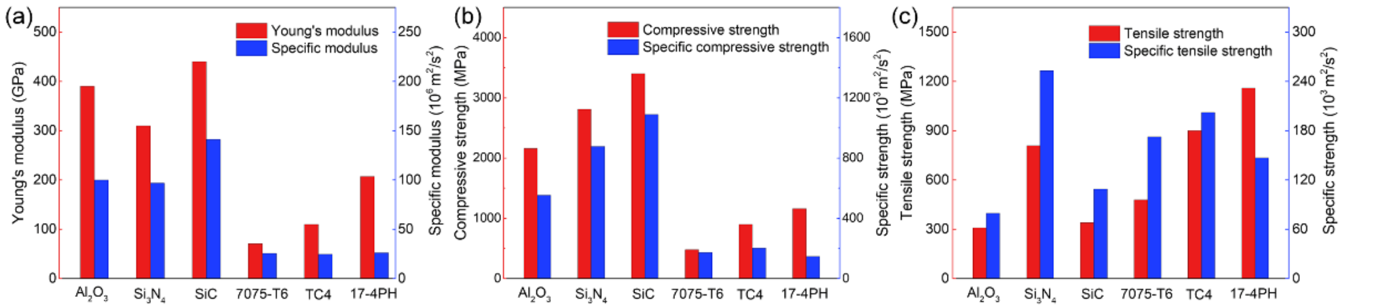

Figure 1. Comparison of materials' mechanical and load-bearing properties. (**a**) Young's modulus vs. specific modulus; (**b**) Compressive strength vs. specific compressive strength; (**c**) Tensile strength vs. specific tensile strength.

2.2. Structure Design

The typical ceramic pressure housing consists of a ceramic cylindrical shell, two hemispherical metal end-caps, two metal U-rings, and epoxy resin adhesive, as shown in Figure 2. The metal U-rings are bonded to both ends of the ceramic shell to protect the end surfaces and act as sealing surfaces. Although the end faces of the ceramic shell can fully meet the sealing requirements by grinding, it has a high probability of being damaged in practical applications. The structure of the metal U-ring has been well documented in the literature [7]. The hemispherical metal end-cap is the most common blocking structure in pressure housings. The holes in the end-caps are required for the interaction of signal and power between the inside and outside of the pressure housing. End-caps are easily manufactured from metal materials, but it is impractical to use ceramic materials due to the high price, long processing period, and poor reliability. Therefore, it is inevitable that the ceramic and metal press against each other under hydrostatic pressure. Then, the Poisson effect occurs, which generates tensile stress on the ceramic contact surfaces.

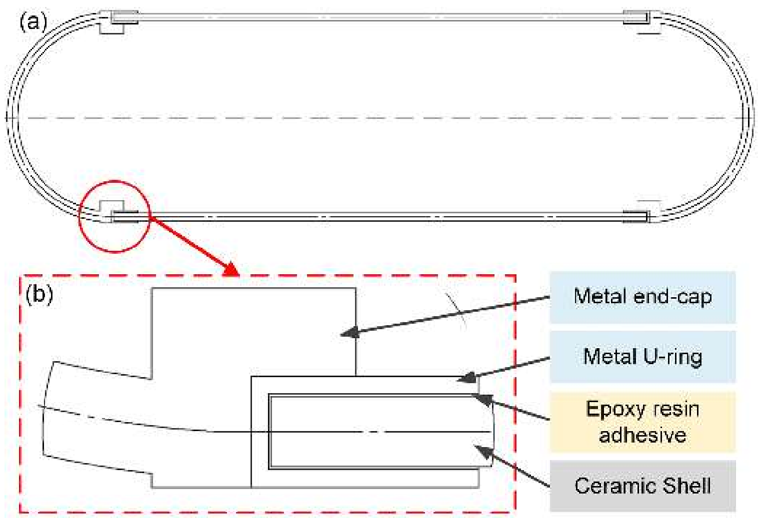

Figure 2. Geometry of a ceramic pressure housing. (**a**) Sectional view; (**b**) Partial view.

3. Mechanical Model

A simplified geometric model of the contact pair is shown in Figure 3. The origin of the cylindrical coordinate system O (r, φ, z) is fixed at the annular center of the unloaded contact plane. The z-axis is the symmetry axis, and the r-axis points outward along the contact surface. After applying the hydrostatic pressure P along the z-axis, a smooth, infinitely rigid flat annular indenter is pressed into the elastic half-space with ε_0. The outer diameter of the ceramic shell is r_o, the inner diameter is r_i, and r_m is the middle diameter.

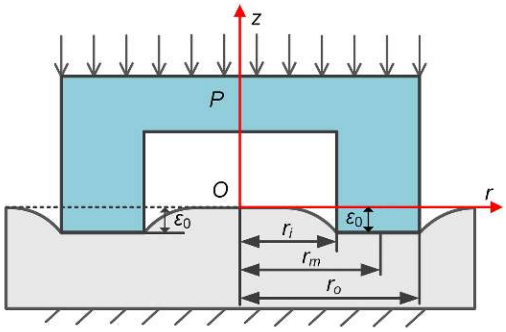

Figure 3. The flat annular indenter pressed into the elastic half-space.

3.1. Frictionless Contact Model of an Infinitely Rigid Flat Annular Indenter

The boundary conditions can be obtained as follows:

$$\begin{cases} (1) & (w_z)_{z=0} = \varepsilon_0, & (r \subseteq [r_i, r_o]) \\ (2) & (\sigma_z)_{z=0} = 0, & (r \subset (0, r_i) \cup (r_o, \infty)) \\ (3) & (\tau_{rz})_{z=0} = 0, & (r \subset (0, \infty)) \end{cases} \tag{1}$$

In addition, neither stress nor displacement exist at infinity. Neglecting the presence of body forces, the equilibrium differential equations for this symmetric elastic displacement are:

$$\begin{cases} 2Gu_r = \frac{\partial \varphi_0}{\partial r} + z\frac{\partial \varphi_3}{\partial r} \\ 2Gw_z = \frac{\partial \varphi_0}{\partial z} + z\frac{\partial \varphi_3}{\partial z} - (3-4v)\varphi_3 \end{cases} \tag{2}$$

where G is the shear modulus and $G = E/(2v + 2)$; v is Poisson's ratio; and E is Young's modulus.

φ_0 and φ_3 are stress functions and satisfy the compatibility conditions:

$$\nabla^2\varphi_0 = \nabla^2\varphi_3 = 0,\ \nabla^2 = \frac{\partial^2}{\partial r^2} + \frac{1}{r}\frac{\partial}{\partial r} + \frac{\partial^2}{\partial z^2} \tag{3}$$

where ∇^2 is the Laplace operator in plane cylindrical coordinates.

To satisfy Condition (3) in Equation (1), the stress functions φ_0 and φ_3 are expressed in cylindrical harmonic form as:

$$\begin{cases} \varphi_0 = -(1-2v)\int_0^\infty \lambda g(\lambda) J_0(\lambda r) e^{-\lambda z} d\lambda \\ \varphi_3 = \int_0^\infty \lambda g(\lambda) J_0(\lambda r) e^{-\lambda z} d\lambda \end{cases} \tag{4}$$

where $g(\lambda)$ is an arbitrary function of λ and $J_v(x)$ is the first type of Bessel function with v order.

Let $z = 0$, and substitute Equation (4) into Equation (2) to obtain the displacement expression of the contact surface, as:

$$\begin{cases} (u_r)_{z=0} = \frac{(1-2v)}{2G}\int_0^\infty g(\lambda) J_1(\lambda r) d\lambda \\ (w_z)_{z=0} = -\frac{(1-v)}{G}\int_0^\infty g(\lambda) J_0(\lambda r) d\lambda = \varepsilon_0 \end{cases} \tag{5}$$

According to the intrinsic relationship between displacement and stress in elastic mechanics, the expression for the stress at the contact surface can be further obtained from Equation (5):

$$\begin{cases} \begin{bmatrix} (\sigma_r)_{z=0} \\ (\sigma_\theta)_{z=0} \end{bmatrix} = \frac{1}{2}\int_0^\infty [(1+2v)J_0(\lambda r) \mp (1-2v)J_2(\lambda r)]\lambda g(\lambda) d\lambda \\ (\sigma_z)_{z=0} = \int_0^\infty \lambda g(\lambda) J_0(\lambda r) d\lambda;\ (\tau_{rz})_{z=0} = 0 \end{cases} \tag{6}$$

Equation (6) is a problem with mixed boundaries in three regions. According to Conditions (1) and (2), the function $g(\lambda)$ can be obtained to satisfy the following relationships:

$$\begin{cases} \int_0^\infty \lambda g(\lambda) J_0(\lambda r) d\lambda = 0, (r \subset (0, r_i) \cup (r_o, \infty)) \\ \int_0^\infty g(\lambda) J_0(\lambda r) d\lambda = -\frac{G\varepsilon_0}{1-v}, (r \subset (r_i, r_o)) \end{cases} \tag{7}$$

Since $(\sigma_z)_{z=0}$ at the contact surface, it has the specificity of $(r^2 - r_i^2)^{-1/2}$ at the inner boundary $r = r_i$ and has the specificity of $(r^2 - r_o^2)^{-1/2}$ at the outer boundary $r = r_o$. It can be assumed that $(\sigma_z)_{z=0}$ has the following form in the annular flat region:

$$(\sigma_z)_{z=0} = -\frac{\varepsilon_0 f(r)}{\sqrt{(r_o^2 - r^2)((r^2 - r_i^2))}}, (r \subseteq [r_i, r_o]) \tag{8}$$

where $f(r)$ is the unknown function but is continuous on $r \subseteq [r_i, r_o]$ and nonzero at the two endpoint positions of the interval. Furthermore, in the interval of $[r_i, r_o]$, two variables r_m and ϕ are set in place of r_i and r_o, denoted as:

$$\begin{cases} r = \sqrt{r_m^2 + b^2 - 2r_m b \cos\phi} \\ r = r_i : \phi = 0;\ r = r_o : \phi = \pi \\ \sqrt{(r_o^2 - r^2)(r^2 - r_i^2)} = 2r_m b \sin\phi \\ r_m = (r_i + r_o)/2;\ b = (r_o - r_i)/2 \end{cases} \tag{9}$$

The function $f(r)$ can be expressed as a Fourier series in the following form:

$$f(r) = \sum_{n=0}^{\infty} a'_n \cos n\phi,\ (r \subseteq [r_i, r_o],\ \phi \subseteq [0, \pi]) \tag{10}$$

According to Equations (9) and (10), Equation (8) can be rewritten as:

$$(\sigma_z)_{z=0} = -\frac{\varepsilon_0}{2r_m b} \sum_{n=0}^{\infty} a'_n \frac{\cos n\phi}{\sin\phi}, (r \subset (r_i, r_o)) \tag{11}$$

Equations (6) and (11) are different expressions of $(\sigma_z)_{z=0}$. Using the condition that the noncontact region $r \subseteq [0, r_i) \cup (r_o, \infty)$, $(\sigma_z)_{z=0} = 0$ and performing the Hankel inverse transformation, $g(\lambda)$ is obtained as:

$$\begin{aligned} g(\lambda) &= -\frac{\varepsilon_0}{2} \sum_{n=0}^{\infty} a'_n \int_0^\pi \cos n\phi J_0(\lambda \sqrt{r_m^2 + b^2 - 2r_m b \cos\phi}) d\phi \\ &= -\frac{\pi\varepsilon_0}{2} \sum_{n=0}^{\infty} a'_n J_n(\lambda r_m) J_n(\lambda b) \end{aligned} \tag{12}$$

Substituting Equation (11) into the second part $(w_z)_{z=0} = \varepsilon_0$ in Equation (5), we obtain:

$$\begin{cases} \sum_{n=0}^{\infty} a_n \int_0^\infty J_n(\lambda r_m) J_n(\lambda b) J_0(\lambda r_m) d\lambda = 1 \\ a_n = \frac{1-v}{2G} \pi a'_n \end{cases} \tag{13}$$

Furthermore, expanding $J_0(\lambda r)$ on $r \subseteq [r_i, r_o]$ into the form of a Fourier series yields:

$$\begin{aligned} J_0(\lambda r) &= J_0(\lambda r_m) J_0(\lambda b) \\ &+2 \sum_{m=1}^{\infty} J_m(\lambda r_m) J_m(\lambda b) \cos(m\phi), (r \subseteq [r_i, r_o], \phi \subseteq [0, \pi]) \end{aligned} \tag{14}$$

Since Equation (14) must be held for any $\phi \subseteq [0,\pi]$, the coefficients a_n are determined by infinitely associating simultaneous equations:

$$\sum_{n=0}^{\infty} a_n \int_0^{\infty} J_n(\lambda r_m) J_n(\lambda b) J_m(\lambda r_m) J_m(\lambda b) d\lambda = \delta_{0,m}, (m = 0, 1, 2, \ldots) \tag{15}$$

where $\delta_{0,\,m}$ is Kronecker's delta (for $\delta_{i,j}$, if $i = j$, then $\delta_{i,j} = 1$; if $i \neq j$, then $\delta_{i,j} = 0$).

Ultimately, the three mixed boundary problem is reduced to solve a set of single infinitely associative one-order equations. Moreover, all displacements and stresses can be calculated once a_n is determined. Equation (12) can be rewritten as an expression containing a_n:

$$g(\lambda) = -\frac{G\varepsilon_0}{1-r} \sum_{n=0}^{\infty} a_n J_n(\lambda r_m) J_n(\lambda b) \tag{16}$$

The displacements and stress at the contact surface are rewritten as:

$$\begin{cases} (u_r)_{z=0} = -\frac{\varepsilon_0(1-2v)}{2(1-v)} \sum\limits_{n=0}^{\infty} a_n I_1 \\ (w_z)_{z=0} = \sum\limits_{n=0}^{\infty} a_n I_0 \\ \begin{pmatrix} \sigma_r \\ \sigma_\theta \end{pmatrix}_{z=0} = \sigma_z \mp \frac{2G(u_r)_{z=0}}{r} \\ (\sigma_z)_{z=0} = -\frac{\varepsilon_0 G}{(1-v)\pi r_m b} \sum\limits_{n=0}^{\infty} a_n \frac{\cos n\phi}{\sin\phi}, (r \subset (r_i, r_o)) \end{cases} \tag{17}$$

where I_0 and I_1 are denoted as:

$$\begin{cases} I_0 = \int_0^{\infty} J_0(\lambda r) J_n(\lambda r_m) J_n(\lambda b) d\lambda \\ I_1 = \int_0^{\infty} J_1(\lambda r) J_n(\lambda r_m) J_n(\lambda b) d\lambda \end{cases} \tag{18}$$

The total load P_{total} is expressed as:

$$P_{total} = -2\pi \int_{r_i}^{r_o} r(\sigma_z)_{z=0} dr = -\frac{2\pi G\varepsilon_0}{1-v} a_0 \tag{19}$$

When the design parameters, such as hydrostatic pressure P and inner and outer diameters r_i and r_o are known, an alternative expression for P_{total} can be obtained as:

$$P_{total} = 2\pi \int_{r_i}^{r_o} rPdr = \pi P(r_o^2 - r_i^2) \tag{20}$$

Therefore, the stress and displacements in Equation (17) can be found, and the specific solution method is referred to in the literature [19].

3.2. Approximate Contact Model of Ceramic Pressure Housing

The calculated stress in Section 3.1 is generated at the contact surface of the elastic half-space. Since the normal stress and normal displacements are equal on both sides of the contact surface in the frictionless contact model:

$$\begin{cases} (\sigma_z^{II})_{z=0} = (\sigma_z)_{z=0}, \ (w_z^{II})_{z=0} = (w_z)_{z=0} \\ (\tau_{rz}^{II})_{z=0} = (\tau_{rz})_{z=0} = 0 \end{cases} \tag{21}$$

where upper corner mark II represents the flat annular indenter, i.e., the ceramic shell.

Due to Poisson's effect, the flat annular ceramic indenter also generates shear traction, which is the source of the tensile stress on the ceramic contact surface. However, the exact tensile stress $(\sigma_r)_{z\,=0}$ cannot be calculated at the moment. Similar to Equation (8), the pressure distribution on the contact surface of the flat annular ceramic indenter can be reasonably approximated by the following equation:

$$p(r) = P_{total} M(\lambda, r_i, r_o) / (r^2 - r_i^2)^{\gamma} (r_o^2 - r^2)^{\gamma} \tag{22}$$

where $p(r)$ is the normal force per unit area, and M (γ, r_i, r_o) is the dimensionless weight function used to satisfy the equilibrium of the forces.

For an infinitely rigid indenter, γ = 0.5, for a finitely rigid one $\gamma \subset$ (0, 0.5), and can be calculated by the following Equation (23):

$$\begin{aligned} &\tan[(1-\gamma)\pi] \sin[(1-\gamma)\pi] \\ &\quad + e\left\{1 - \cos[(1-\gamma)\pi] - 2(1-\gamma)^2\right\} = 0 \end{aligned} \tag{23}$$

where e is equal to Young's modulus of the indenter divided by Young's modulus of the half-space, i.e., $e = E_c / E_m$.

In Equation (23), the difference in Poisson's ratio is not considered. The literature [23] verifies that the error at extreme differences in Poisson's ratio is less than 5%. A more precise but complex formula is given in the literature [25].

When γ = 0.5, combining Equations (8) and (22), one can obtain:

$$\left(\sigma_z^{II}\right)_{z=0} = -\frac{\varepsilon_0 f(r)}{\sqrt{(r_o^2 - r^2)((r^2 - r_i^2))}} = \frac{P_{total} M(\lambda, r_i, r_o)}{(r^2 - r_i^2)^{\gamma} (r_o^2 - r^2)^{\gamma}}, (r \subseteq [r_o, r_i]) \tag{24}$$

Furthermore, the dimensionless weight function M (γ, r_i, r_o) can be obtained as follows:

$$M(\lambda, r_i, r_o) = -\frac{2\varepsilon_0 G \sum\limits_{n=0}^{\infty} a_n \cos n\phi}{(1-v)\pi^2 P (r_o^2 - r_i^2)}, (r \subseteq [r_o, r_i]) \tag{25}$$

By bringing Equation (25) into Equation (24), the rewritten Equation (26) is obtained:

$$(\sigma_z^{II})_{z=0} = p(r) = -\frac{2\varepsilon_0 G \sum\limits_{n=0}^{\infty} a_n \cos n\phi}{(1-v)\pi^2 (r^2 - r_i^2)^{\gamma} (r_o^2 - r^2)^{\gamma}}, (r \subseteq [r_o, r_i]) \tag{26}$$

From Equation (26), it can be seen that the solution is also transformed into solving for a_n.

Then, the contact surface tensile stress of the ceramic shell can be calculated:

$$\left(\sigma_r^{II}\right)_{z=0} = \kappa(\sigma_z^{II} - \frac{2Gu_r^{II}}{r}) \tag{27}$$

where κ is the structure coefficient and represents the effect of the difference between the actual and simplified structures on the magnitude of tensile stress.

4. Model Validation

4.1. Preliminary Design

The three ceramic materials and three metal materials listed in Table 1 are combined to produce nine groups of ceramic pressure housings. The length of the ceramic hull L_c and the inner diameter $D_{c\text{-}i}$ are set to 800 mm and 287 mm, respectively. To ensure effective stress transmission, the middle diameter of the pressure shell $D_{c\text{-}m}$ is set equal to the middle diameter of hemispherical end-cap $D_{s\text{-}m}$. The ceramic pressure housings are preliminarily designed with respect to the aspects of compressive strength and buckling.

The wall thickness t_c of the ceramic shell is calculated by Equation (28):

$$\begin{cases} t_{c\text{-}str} = D_{c\text{-}i}(-1 + 1/\sqrt{1 - 2f_{c\text{-}str}P_{sea}/\sigma_c})/2 \\ t_{c\text{-}buck} = D_{c\text{-}i}^{1.4}(P_{sea}f_{c\text{-}buck}/(2.59EL))^{0.4} \\ t_c = \max\{t_{c\text{-}str}, t_{c\text{-}buck}\} \\ D_{c\text{-}m} = D_{s\text{-}m} = D_{c\text{-}i} + t_c \end{cases} \tag{28}$$

The wall thickness t_s of the hemispherical metal end-cap can be calculated by Equation (29):

$$\begin{cases} t_{s\text{-}str} = D_{s\text{-}m}P_{sea}/(4f_{s\text{-}str}\sigma_s) \\ t_{s\text{-}buck} = D_{s\text{-}m}(2kf_{s\text{-}buck}P_{sea}E)^{0.5}(3(1-\mu^2))^{0.25}/(4E) \\ t_s = \max\{t_{s\text{-}str}, t_{s\text{-}buck}\} \end{cases} \tag{29}$$

where $f_{c\text{-}str}$ and $f_{c\text{-}buck}$ are the compressive strength and buckling safety factor of the ceramic cylindrical shell, respectively; $f_{s\text{-}str}$ and $f_{s\text{-}buck}$ are the compressive strength and buckling safety factor of the hemispherical metal end-cap, respectively. Usually, the above-mentioned safety factors can be taken as 1.3, and k is the actual load failure factor, tested at 0.7 [26]. The design pressure P_{sea} is set to 115 MPa, which is the hydrostatic pressure in the deepest part of the world's oceans. The calculation results for nine groups of ceramic pressure housings are shown in Table 2 and are rounded around the safety factors.

Table 2. Preliminary design dimensions of the nine groups of ceramic pressure housings.

No.	Groups	L_c (mm)	$D_{c\text{-}I}$ (mm)	$D_{c\text{-}m}/D_{s\text{-}m}$ (mm)	t_c (mm)	t_s (mm)
1	SiC&7075-T6	800	287	299	12.0	22.4
2	SiC&TC4	800	287	299	12.0	12
3	SiC&17-4PH	800	287	299	12.0	9.2
4	Al_2O_3&7075-T6	800	287	299.5	12.5	22.4
5	Al_2O_3&TC4	800	287	299.5	12.5	12
6	Al_2O_3&17-4PH	800	287	299.5	12.5	9.2
7	Si_3N_4&7075-T6	800	287	300.8	13.8	22.4
8	Si_3N_4&TC4	800	287	300.8	13.8	12
9	Si_3N_4&17-4PH	800	287	300.8	13.8	9.2

Table 2 shows that once the preliminary design requirements (length, inner diameter, design pressure, etc.) are determined, the shell thickness is very close. This is due to the high specific compressive strength and modulus properties of the ceramic materials. Therefore, the structure coefficient κ of the nine sets of housings in the approximate model can be considered a constant value. In this paper, $\kappa = \sigma_{r\_model}/\sigma_{r\_FEM}$, where σ_{r_model} is the maximum tensile stress of the simplified pressure housing calculated by the finitely rigid flat annular indenter model and σ_{r_FEM} is the maximum tensile stress of the practical pressure housing calculated by FEM simulations. Then, κ of any group of housings can be used as κ of all nine groups for the approximation of the model.

The mechanical properties of the epoxy resin adhesive used in the actual model are shown in Table 3.

Table 3. Properties of the epoxy resin adhesive.

Description	Specific Gravity	Shear Modulus	Flexural Stress	Poisson's Ratio	Flexural Modulus
Value	1.05 g/cm^3	1.3 GPa	60 MPa	0.40	1.9 GPa

4.2. FEM Simulations

The finite element method simulation is used for the verification of the approximate model. In this paper, the simulation tool used is the commercial software ANSYS Workbench. The ceramic pressure housing is a typical axisymmetric rotating body. By reducing the dimensions and using an axisymmetric analysis of the ceramic pressure housing, we can effectively reduce the calculation costs and obtain a higher level of accuracy. In addition, in Ansys Workbench, the mesh and analysis results in three-dimensional states can be obtained by "Symmetry". The mesh of the contact area is further refined to obtain higher local calculation accuracy. Figure 4 shows a ceramic pressure housing mesh with "Symmetry". The grid numbers of the nine groups of ceramic pressure housings range from 249,147 to 277,924, with an average of 262,928, and the number of nodes ranges from 766,514 to 853,087, with an average of 807,927. The contact regions at one end of the ceramic pressure housing include the "metal U-ring and metal end-cap", "metal U-ring and epoxy resin adhesive" and "epoxy resin adhesive and ceramic shell end face". Since the metal U-ring and the metal end-cap are fastened by multiple bolts in practice, the contact type of the contact region in ANSYS Workbench can be regarded as "bond". In addition, the other two contact regions are adhesive surfaces, which are also set to the "bond" contact type. Hydrostatic pressure of 115 MPa is applied uniformly outside the ceramic pressure housings.

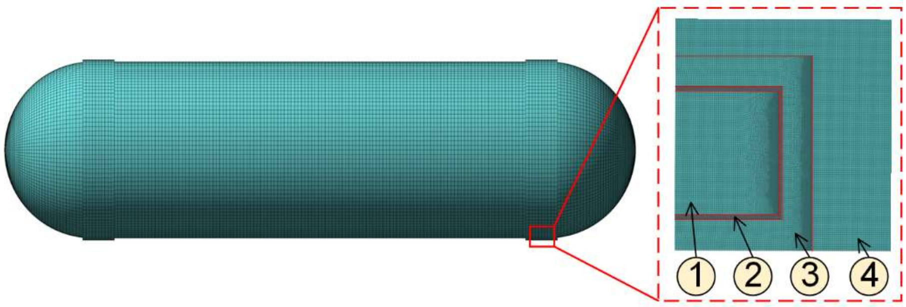

Figure 4. The mesh of a ceramic pressure housing with "Symmetry", (1) ceramic shell, (2) epoxy resin adhesive, (3) mental U-ring and (4) metal end-cap.

5. Results and Discussion

5.1. Bearing Capacity

The weight-to-displacement ratio (W/D) of a ceramic pressure housing can be obtained by Equation (30):

$$\eta = \frac{M}{\rho_{sea\_0} V} \tag{30}$$

where M is the total mass of a ceramic pressure housing and V is its displacement volume; ρ_{sea_0} is the sea water density at the surface and can be approximated as 1021 kg/m^3; η is a dimensionless value, and the smaller it is, the more the housing is capable of carrying.

The wall thickness of the metal U-ring is set to 3 mm, and the slot depth is set to 36 mm (approximately 2.5 times the wall thickness of the ceramic shell). The W/D of the nine groups of ceramic pressure housings and ceramic shells (including two bonded metal U-rings) are calculated and shown in Figure 5. Based on the preliminary design, the SiC ceramic pressure housings and shells have better W/D than the Al_2O_3 and Si_3N_4 ceramic pressure housings and shells. This is because the specific modulus and specific compressive strength of the SiC ceramic are the best among the three ceramic materials (see Table 1). The optimal combination is SiC&7075-T6, with W/D values of 0.685 and 0.45 for the housing and ceramic shell, respectively. Although the use of metal components enhances reliability, it weakens the W/D performance of the ceramic pressure housing.

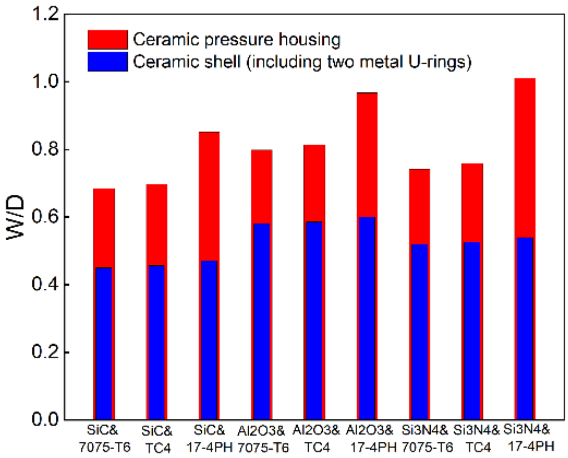

Figure 5. The W/D of the nine groups of ceramic pressure housings and ceramic shells.

5.2. Tensile Stress on Ceramic Contact Surfaces

Figure 6 shows the tensile stress simulation results of the nine groups of ceramic pressure housings at 115 MPa hydrostatic pressure, which is represented by the maximum principal stress, where Figure 6a–c are SiC&7075-T6, SiC&TC4, and SiC&17-4PH, respectively; Figure 6d–f are Al_2O_3&7075-T6, Al_2O_3&TC4, and Al_2O_3&17-4PH, respectively; Figure 6g–i are Si_3N_4&7075-T6, Si_3N_4&TC4, and Si_3N_4&17-4PH, respectively. The results show that the maximum tensile stress occurs at the contact surface near the inner boundary of the ceramic shell. At the same hydrostatic pressure, a ceramic shell combined with different metals will have different values of contact tensile stress. This also indicates that there are different tensile stress safety factors for ceramic shell contact with different metals. This provides guidance on the material selection for ceramic pressure housings.

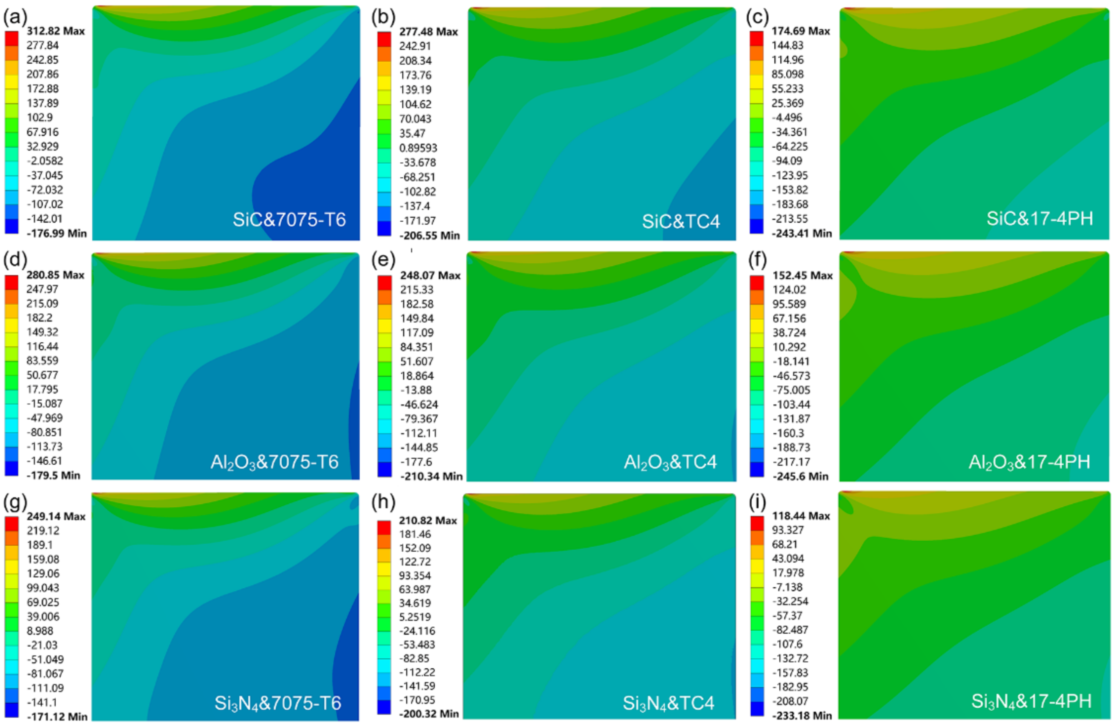

Figure 6. The tensile stress on the nine groups of ceramic contact faces at the preliminary designed dimensions and hydrostatic pressure of 115 MPa. (**a**–**c**) SiC&7075-T6, SiC&TC4, and SiC&17-4PH; (**d**–**f**) Al_2O_3&7075-T6, Al_2O_3&TC4, and Al_2O_3&17-4PH; (**g**–**i**) Si_3N_4&7075-T6, Si_3N_4&TC4, and Si_3N_4&17-4PH.

Table 4 shows the structure coefficients κ calculated from the nine groups, with a maximum deviation of 14.2%; this means that the results calculated by the approximate model using the structure coefficients obtained from any one group of numerical simulations have an absolute error of no more than 14.2%.

Table 4. γ and κ for the nine groups of ceramic pressure housings.

Groups	SiC& 7075-T6	SiC& TC4	SiC& 17-4PH	Al_2O_3& 7075-T6	Al_2O_3& TC4	Al_2O_3& 17-4PH	Si_3N_4& 7075-T6	Si_3N_4& TC4	Si_3N_4& 17-4PH
γ	0.416	0.382	0.317	0.408	0.371	0.303	0.389	0.348	0.276
κ	2.97	2.75	2.99	3.14	2.90	2.97	2.87	2.79	3.14

The calculated results for the approximate model in Figure 7 use the structure coefficient of SiC&7075-T6, κ = 2.97, and the structure coefficient of Si_3N_4&17-4PH, κ = 3.14. The results of FEM simulations in Figure 7 show that the highest safety factor is the Si_3N_4 ceramic pressure housing, with safety factors from 3.2 to 7. The lowest safety factor occurs in the SiC ceramic pressure housings. Among the nine groups of ceramic pressure housings, there are four groups below the initial design safety factor (1.3). They are SiC&7075-T6, SiC&TC4, Al_2O_3&7075-T6, and Al_2O_3&TC4, with safety factors of 1.08, 1.22, 1.1, and 1.25, respectively. The maximum errors calculated by the approximate model are 11.2% and 14.2%.

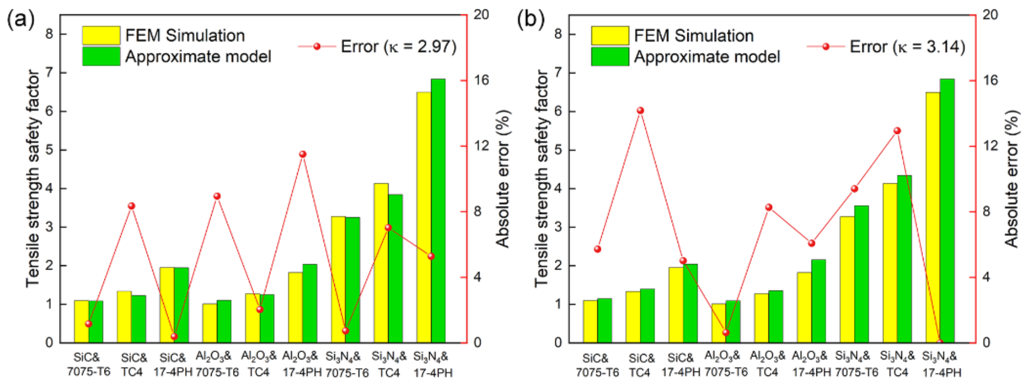

Figure 7. Tensile strength safety factor and its absolute error for nine groups of ceramic pressure housings. (**a**) κ = 2.97; (**b**) κ = 3.14.

The linearized distribution of the tensile stress on the ceramic contact surface along the wall thickness direction is shown in Figures 8–10, where r_c = 0 represents the boundary of $r = r_i$. Figures 8–10 show the results of three groups of SiC ceramic pressure housings, three groups of Al_2O_3 ceramic pressure housings, and three groups of Si_3N_4 ceramic pressure housings, respectively. The results of the approximate model (κ = 2.97) and FEM simulations indicate that the smaller the difference in Young's modulus of the materials, the lower the tensile stress on the ceramic contact surface. In addition, there are concentrations of tensile stress near the two boundaries of the ceramic contact surface. It can also be concluded that the most likely region of failure is near the inner boundary of the ceramic shell.

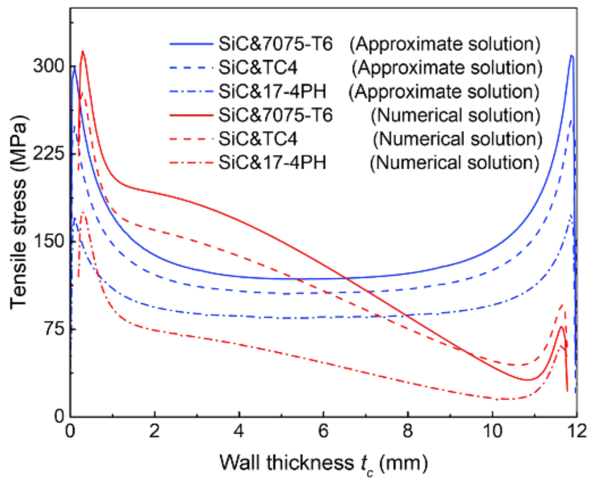

Figure 8. Linearized distribution of tensile stress on the contact surface along the wall thickness (three groups of SiC ceramic pressure housings).

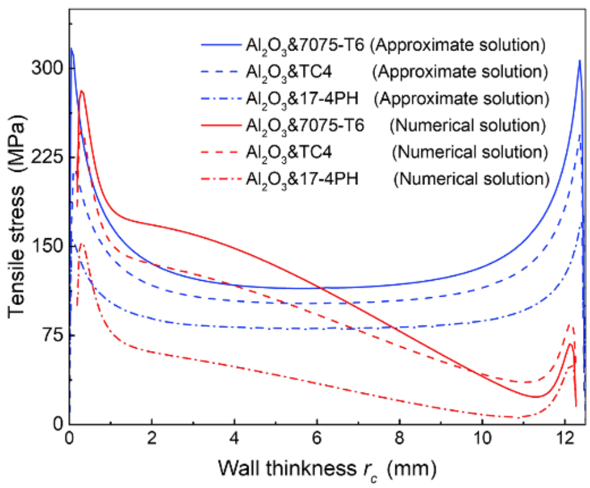

Figure 9. Linearized distribution of tensile stress on the contact surface along the wall thickness (three groups of Al_2O_3 ceramic pressure housings).

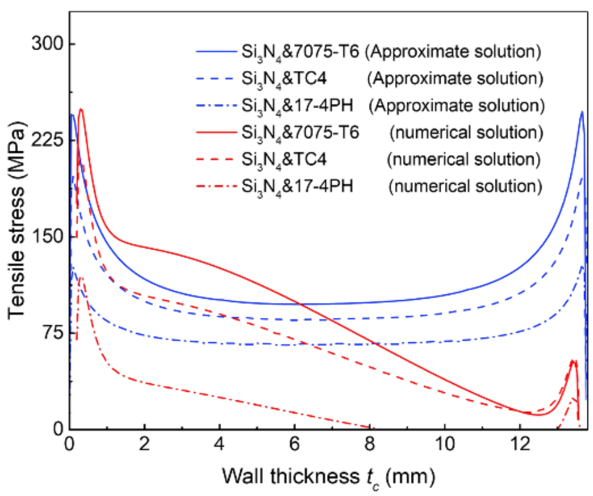

Figure 10. Linearized distribution of tensile stress on the contact surface along the wall thickness (three groups of Si_3N_4 ceramic pressure housings).

The results of the FEM simulations also show that the tensile stress in the middle part of the wall thickness has a decreasing trend along the *r*-axis outward, which is different from the approximate model. The ends of the ceramic shell are supported by the metal end-caps, resulting in the uneven deformation of the shell along the radial direction under hydrostatic pressure. This leads to a "tilt" phenomenon of contact surface deformation along the axial direction. Unfortunately, it is not reflected in the approximation model.

5.3. Hydrostatic Pressure Experiments

We first test the SiC&7075-T6 ceramic pressure housing with the best W/D among the nine groups. The tensile strength safety factors calculated by the FEM simulation and the approximate model are all close to 1.1. The maximum pressure is set to 115 MPa. A cyclic pressure test under 0~–115 MPa is planned. The high-pressure chamber (see Figure 11a is capable of meeting the pressure experiment. A significant pressure drop is found approximately ten minutes after entering 115 MPa. The SiC&7075-T6 ceramic pressure housing removed from the high-pressure chamber is shown in Figure 11b,c. A penetration crack (Crack 1) appears in the pressure housing, oriented along the cylindrical bus. Another crack (Crack 2) appears in the middle of the pressure housing and is nearly perpendicular to Crack 1.

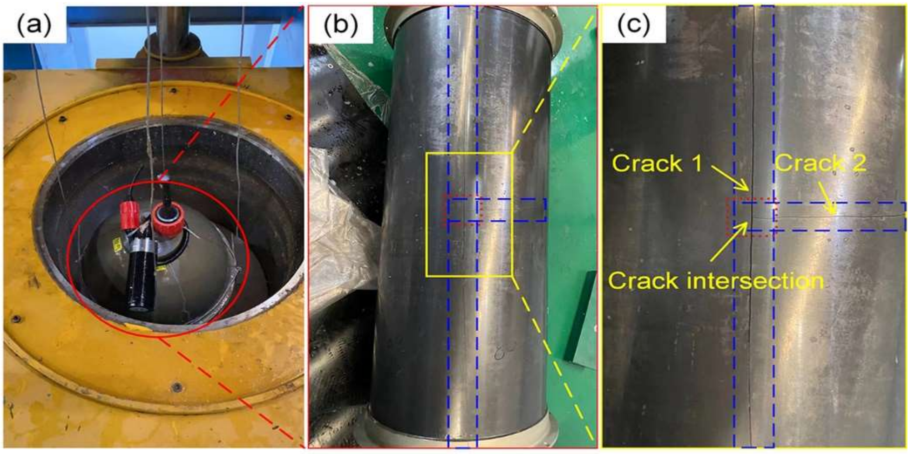

Figure 11. Hydrostatic pressure experiment for the SiC&7075-T6 ceramic pressure housing. (**a**) The SiC&7075-T6 ceramic pressure housing loaded into the high-pressure chamber; (**b**) Failed pressure housing; (**c**) Partial view of the failed pressure housing with two cracks.

It is clear that Crack 1 is generated by the failure of the tensile strength in the contact surface, which is the typical failure form of ceramic pressure housings. This result verifies that the failure of the ceramic pressure housings is very different from that of the metal housings. Crack 2 arises on one side of the ceramic shell and is not symmetrical, indicating that it is accompanied by Crack 1 rather than being the first crack to fail. The maximum radial displacement and maximum compressive stress are generated in the middle of the ceramic pressure housing under uniform hydrostatic external pressure. Therefore, this area is more likely to produce accompanying cracks during the growth of penetration cracks on the contact surface; such cracks occur in a short period of time.

Another hydrostatic pressure experiment verified the SiC&TC4 pressure housing, as shown in Figure 12a. The support structure of the metal end-cap is optimized [27], and the wall thickness of the ceramic shell is increased appropriately. Thus, the safety of the SiC&TC4 pressure housing is further improved (see Table 5). Due to the capabilities of the high-pressure chamber, the maximum pressure is only raised to 110 MPa. Eventually, the hydrostatic pressure test is performed for three cycles from 0 to 110 MPa in approximately 45 min (see Figure 12b). The results show that the pressure curve barely drops during the 110 MPa pressure-holding process. This indicates that the SiC&TC4 ceramic pressure housing meets the design requirements. Moreover, its W/D is the best among the nine groups of ceramic pressure housings except for SiC&7075-T6.

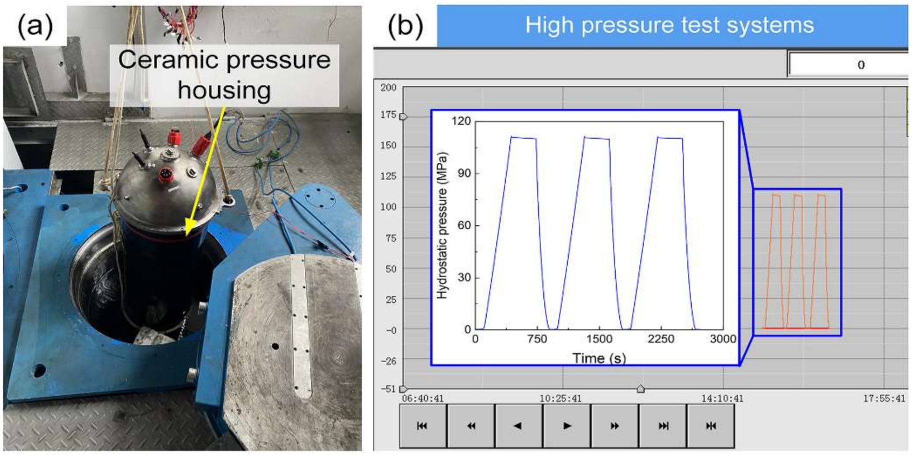

Figure 12. Hydrostatic pressure experiment of the SiC&TC4 ceramic pressure housing. (**a**) SiC&TC4 ceramic pressure housing loaded into the high-pressure chamber; (**b**) Hydrostatic pressure curve (three cycles from 0 to 110 MPa).

Table 5. Comparison with other 11,000 m class ceramic pressure housings.

Description	Materials	$D_{c\text{-}o}/L_c/t_c$ (mm)	W/D	Safety Facter	Applications
Stachiw et al. [7] and	96% AL2O3&TC4	355/432/15.2	0.58	1.5	"Nereus" HROV
Bowen et al. [8]	96% AL2O3&TC4	191/435/10	0.70	1.5	"Nereus" HROV
This work	SiC&TC4	314/800/13.5	0.52	1.5	"Petrel-X $^{\text{PLUS}}$" HG

In July 2020, the "Petrel-X $^{\text{PLUS}}$" hadal glider (HG), developed by Tianjin University, China, using the SiC&TC4 ceramic pressure housing, successfully dived to a depth of 10,619 m in the Challenger Deep, Marianas Trench [28]. We compared our ceramic pressure housing with that of the "Nereus" HROV, as they are in practical use on FOD submersibles. The comparison results in Table 5 show that our housing has a better W/D, i.e., a better carrying capacity. This further validates the great potential of ceramic pressure housings for FOD submersible applications.

6. Conclusions

This paper analyzes the tensile stress calibration of ceramic pressure housings by an approximate mechanical model, FEM simulations, and hydrostatic pressure experiments. The approximate mechanical model is established using contact mechanics. FEM simulations of nine groups of pressure-resistant shells were carried out for approximate model verification. Finally, experimental verification was conducted by two hydrostatic pressure experiments. The following conclusions were drawn:

1. The approximate model proposed in this paper has acceptable errors when analyzing the tensile stress on the ceramic contact surface. Among the nine groups of ceramic pressure housings, the absolute errors between the approximation model and FEM simulations are no more than 14.2%.
2. The results of the approximate model and FEM simulations for nine groups of ceramic pressure housings show that the smaller the difference in Young's modulus between the ceramic and metal, the lower the tensile stress on the contact surface. The maximum tensile stress on the ceramic contact surface occurs close to the inner boundaries ($r = r_i$), which provides guidance for subsequent structure optimization. The contact faces of the ceramic pressure housing can be redesigned to achieve an

equivalent tensile stress distribution to prevent localized tensile stress from exceeding the ceramic's limit.

3. The results of hydrostatic pressure experiments show that the ceramic pressure housing may fail even with a safety factor of slightly greater than 1. Due to the complexity of the adhesive process, the dimensional accuracy of the contact region is difficult to control. The actual tensile stress on the ceramic contact surface under hydrostatic pressure is difficult to calculate accurately. Therefore, the selection of the tensile stress safety factor must be given a greater margin. In this paper, we recommend 1.5~–2.

Future work will further quantify the adhesive effects and perform an equivalent tensile stress design for ceramic shell end surfaces. It is essential to exploit the very high pressure-bearing properties of ceramic materials. Meanwhile, it is of great importance to enhance the carrying capacity of FOD submersibles and to promote hadal observations.

Author Contributions: Conceptualization, P.W. and Y.W.; methodology, P.W.; software, P.W., X.W. and P.L.; validation, P.W., Y.W. and S.Y.; formal analysis, W.N.; writing—original draft preparation, P.W.; writing—review and editing, Y.W., X.W., W.N. and S.Y.; funding acquisition, Y.W. All authors have read and agreed to the published version of the manuscript.

Funding: This work was jointly supported by the National Key R&D Program of China, grant No. 2019YFC0311803; the National Natural Science Foundation of China, grant No. 51721003; Natural Science Foundation of Tianjin City, grant No. 18JCJQJC46400; and Aoshan Talent Cultivation Program, grant Nos. 2017ASTCP-OS05 and 2017ASTCP-OE01 of QNLM.

Institutional Review Board Statement: Not applicable.

Informed Consent Statement: Not applicable.

Data Availability Statement: Data are not publicly available.

Conflicts of Interest: The authors declare no conflict of interest.

References

1. Jamieson, A.J.; Fujii, T.; Mayor, D.J.; Solan, M.; Priede, I.G. Hadal trenches: The ecology of the deepest places on Earth. *Trends Ecol. Evol.* **2010**, *25*, 190–197. [CrossRef] [PubMed]
2. Agostini, V.; Arico, S.; Briones, E.; Clark, M.; Cresswell, I.; Gjerde, K.; Grant, S.; Niewijk, D.; Polacheck, A.; Rice, J. *Global Open Oceans and Deep Seabed (GOODS) Biogeographic Classification*; UNESCO-IOC Technical Series; UNESCO-IOC: Paris, France, 2009; Volume 84.
3. Du, M.; Peng, X.; Zhang, H.; Ye, C.; Dasgupta, S.; Li, J.; Li, J.; Liu, S.; Xu, H.; Chen, C.; et al. Geology, environment, and life in the deepest part of the world's oceans. *Innovation* **2021**, *2*, 100–109. [CrossRef] [PubMed]
4. Jamieson, A.J. Ecology of deep oceans: Hadal trenches. In *eLS*; Wiley: Hoboken, NJ, USA, 2011.
5. LaSalvia, J.C.; Campbell, J.; Swab, J.; McCauley, J. Beyond hardness: Ceramics and ceramic-based composites for protection. *Jom* **2010**, *62*, 16–23. [CrossRef]
6. Otitoju, T.A.; Okoye, P.U.; Chen, G.; Li, Y.; Okoye, M.O.; Li, S. Advanced ceramic components: Materials, fabrication, and applications. *J. Ind. Eng. Chem.* **2020**, *85*, 34–65. [CrossRef]
7. Stachiw, J.; Peters, D.; McDonald, G. Ceramic external pressure housings for deep sea vehicles. In Proceedings of the OCEANS 2006, Singapore, 16–19 May 2006; pp. 1–7.
8. Bowen, A.D.; Yoerger, D.R.; Taylor, C.; McCabe, R.; Howland, J.; Gomez-Ibanez, D.; Kinsey, J.C.; Heintz, M.; McDonald, G.; Peters, D.B. The Nereus hybrid underwater robotic vehicle for global ocean science operations to 11,000 m depth. In Proceedings of the OCEANS 2008, Quebec City, QC, Canada, 15–18 September 2008; pp. 1–10.
9. Asakawa, K.; Nakamura, M.; Maeda, Y.; Hyakudome, T.; Ishihara, Y. Development of underwater glider for long-term virtual mooring: Aiming 6000 m depth with ceramic housing. In Proceedings of the 2016 Techno-Ocean (Techno-Ocean), Kobe, Japan, 6–8 October 2016; pp. 419–424.
10. Sun, S.; Chen, F.; Zhao, M. Numerical simulation and analysis of the underwater implosion of spherical hollow ceramic pressure hulls in 11,000 m depth. *J. Ocean Eng. Sci.* **2022**. [CrossRef]
11. Zhang, X.; Feng, M.; Zhao, M.; Zhang, P.; He, C.; Qi, H.; Han, W.; Guo, F. Failure of silicon nitride ceramic flotation spheres at critical state of implosion. *Appl. Ocean Res.* **2020**, *97*, 102080. [CrossRef]
12. Asakawa, K.; Hyakudome, T.; Yoshida, M.; Okubo, N.; Ito, M.; Terada, I. Ceramic Pressure-Tight Housings for Ocean-Bottom Seismometers Applicable to 11-km Water Depth. *IEEE J. Ocean. Eng.* **2012**, *37*, 756–763. [CrossRef]

13. Johnson, R.P.; Kurkchubasche, R.; Stachiw, J.D. *Naval Command Control and Ocean Surveillance Center RDT and E DIV San Diego CA. Effect of Different Axial Bearing Supports on the Fatigue Life of Ceramic Pressure Housings*; Defense Technical Information Center: Fort Belvoir, VA, USA, 1993.
14. Takagawa, S. New ceramic pressure hull design for deep water applications. In Proceedings of the OCEANS'10 IEEE SYDNEY, Sydney, Australia, 24–27 May 2010; pp. 1–6.
15. Danzer, R. On the relationship between ceramic strength and the requirements for mechanical design. *J. Eur. Ceram. Soc.* **2014**, *34*, 3435–3460. [CrossRef]
16. Pouraliakbar, H.; Monazzah, A.H.; Bagheri, R.; Reihani, S.S.; Khalaj, G.; Nazari, A.; Jandaghi, M. Toughness prediction in functionally graded Al6061/SiCp composites produced by roll-bonding. *Ceram. Int.* **2014**, *40*, 8809–8825. [CrossRef]
17. Rafieipour, M.H.; Nazari, A.; Mohandesi, M.A.; Khalaj, G. Improvement compressive strength of cementitious composites in different curing media by incorporating ZrO_2 nanoparticles. *Mater. Res.* **2012**, *15*, 177–184. [CrossRef]
18. Collins, W. On the solution of some axisymmetric boundary value problems by means of integral equations: VIII. Potential problems for a circular annulus. *Proc. Edinburgh Math. Soc.* **1963**, *13*, 235–246. [CrossRef]
19. Shibuya, T.; Koizumi, T.; Nakahara, I. An elastic contact problem for a half-space indented by a flat annular rigid stamp. *Int. J. Eng. Sci.* **1974**, *12*, 759–771. [CrossRef]
20. Willert, E.; Li, Q.; Popov, V.L. The JKR-adhesive normal contact problem of axisymmetric rigid punches with a flat annular shape or concave profiles. *Facta Univ. Ser. Mech. Eng.* **2016**, *14*, 281–292. [CrossRef]
21. Popov, V.L.; Heß, M.; Willert, E. *Handbook of Contact Mechanics: Exact Solutions of Axisymmetric Contact Problems*; Springer Nature: Berlin, Germany, 2019.
22. Ciavarella, M. An approximate JKR solution for a general contact, including rough contacts. *J. Mech. Phys. Solids* **2018**, *114*, 209–218. [CrossRef]
23. Jordan, E.H.; Urban, M.R. An approximate analytical expression for elastic stress in flat punch problems. *Wear* **1999**, *236*, 134–143. [CrossRef]
24. McDonald, G. Operations to 11,000 m: Nereus ceramic housing design and analysis. In Proceedings of the 2013 OCEANS-San Diego, San Diego, CA, USA, 23–27 September 2013; pp. 1–5.
25. Gdoutos, E.; Theocaris, P. Stress concentrations at the apex of a plane indenter acting on an elastic half plane. *J. Appl. Mech.* **1975**, *42*, 688–692. [CrossRef]
26. Pan, B.; Cui, W. An overview of buckling and ultimate strength of spherical pressure hull under external pressure. *Mar. Struct.* **2010**, *23*, 227–240. [CrossRef]
27. Wang, P.; Wang, Y.; Yang, S.; Niu, W.; Wang, X.; Liu, X. Effects of Hemispherical End-caps Geometric Optimization on Fatigue Life of Ceramic External Pressure Housing. In Proceedings of the Global Oceans 2020, Singapore, 5–30 October 2020; pp. 1–5.
28. Chinese Underwater Glider Smashes World Record with 10,000-Meter Deep-Water Descent. Available online: http://www.chinesetoday.com/en/article/1295572 (accessed on 13 March 2022).